

Research Article

Experimental Investigation on Sandstone Permeability under Plastic Flow: Permeability Evolution Law with Stress Increment

Peng Gong ¹, Xiaoyan Ni ^{1,2}, Zhanqing Chen ¹, Yu Wu ¹ and Jiangyu Wu¹

¹State Key Laboratory for Geomechanics and Deep Underground Engineering, School of Mechanics and Civil Engineering, China University of Mining & Technology, Xuzhou, Jiangsu 221116, China

²School of Architectural Construction, Jiangsu Vocational Institute of Architectural Technology, Xuzhou 221116, China

Correspondence should be addressed to Xiaoyan Ni; nxyandff@126.com

Received 17 February 2019; Accepted 21 April 2019; Published 26 June 2019

Academic Editor: Baojun Bai

Copyright © 2019 Peng Gong et al. This is an open access article distributed under the Creative Commons Attribution License, which permits unrestricted use, distribution, and reproduction in any medium, provided the original work is properly cited.

Permeability is an important physical property of rock. In rock and rock-like materials, permeability after yielding is closely related to plastic flow behavior. Theoretical analysis and experimental investigations are effective and reliable ways of studying the evolution of permeability. In this paper, fluid flow tests of sandstone samples under 11 stress states were conducted using the MTS 816.02 rock mechanics testing system and a self-designed permeation system. A new plastic flow rule was proposed based on the Mohr-Coulomb yield criterion and a nonassociated flow rule. The applicability of the flow rule was verified by comparing the estimated and experimental values of the equivalent shear strain of the Mohr-Coulomb criterion. Two new coefficients were defined to reflect the influence of the volume deformation and shear deformation on the permeability. A permeability model for plastic flow was established, which can be used to calculate both single-step and multistep permeability estimates of the sandstone samples during plastic flow. The errors of both estimation methods were analyzed. The experimental results showed that the plastic multiplier for the sandstone samples was positive during unloading conditions and negative during loading conditions. The experimental value error of the single-step permeability estimation was less than 16.5%. The experimental value errors of the multistep permeability estimations varied between 15.6% and 16.7%, indicating that the iterative format of the multistep permeability estimation method was generally stable and highly precise. A comparison of the permeability influence coefficients indicated that the influence of the equivalent shear strain on the permeability was smaller than that of the volumetric strain.

1. Introduction

Sandstone is the primary type of sedimentary rock in which rock engineering problems arise, such as water disasters in coal mining engineering. Water inrush through roof or floor sandstone aquifers has become a serious problem that occurs in some deep coal mines [1].

Water inrush can happen in coal mines when roof or floor sandstone aquifers have well-connected major flow paths. Fluid flow research of sandstone roof or floor under mining-induced stress conditions is the fundamental study on water inrush. The permeability evolution of sandstone is the key to studying the fluid flow behavior under mining. In the process of coal mining, deformation on the sandstone

roof and floor is dominated by plastic displacements. Therefore, investigating the permeability evolution of sandstone under plastic deformation is essential.

Permeability, the ability to transmit fluid is one of the most important physical properties of sandstone [2–4]. The evolution of permeability is associated with certain rock characteristics, and numerous researchers have attempted to correlate permeability with these characteristics. Some studies noted that the permeability of rocks is closely related to their porosity characteristics [5–9].

Keynon [10] proposed a power-law relationship between permeability and porosity:

$$k = a\phi^b, \quad (1)$$

where ϕ is porosity, k is permeability, b is a power exponent, and a is the limit of permeability when porosity tends to zero, i.e., $a = \lim_{\phi \rightarrow 0} k$.

Pape et al. [11] identified a relationship between the porosity and permeability of Rotliegend sandstone from a large dataset of experimental test results:

$$k = 3.10 \times 10^{-11} \phi + 7.46 \times 10^{-09} \phi^2 + 1.91 \phi^{10}. \quad (2)$$

Currently, the permeability-porosity relationship defined by rational fractions is the most widely used [12]:

$$k = k_0 \left(\frac{1 - \phi_0}{1 - \phi} \right)^2 \left(\frac{\phi}{\phi_0} \right)^3, \quad (3)$$

where ϕ_0 is the initial porosity, and k_0 the initial permeability, i.e., $k_0 = k|_{\phi=\phi_0}$.

Rock deformation can result in a permeability change. Some experimental studies were conducted by researchers to investigate the deformation and permeability characteristics of rocks and to try to establish a relationship between permeability and strain. Main et al. [13] presented a simple geometrical model of the permeability changes due to increasing inelastic axial strain based on laboratory experiments. The model quantitatively explained the entire permeability cycle observed in the sandstone samples. Wang and Park [14] investigated the permeability of sedimentary rocks during the complete strain-stress process in a triaxial compression test. From the experimental results, they characterized the permeability into five stages according to the axial strain.

Many researchers have investigated the relationship between rock permeability and stress components [15–22].

The empirical expression between permeability and the effective normal stress was obtained by Louis [23] from water-drilling test data at a dam site:

$$k = k_0 \exp(-a_2 \sigma), \quad (4)$$

where σ is the effective normal stress and a_2 is the coefficient to be determined.

Snow [24] conducted a set of seepage tests of parallel fractures and proposed the following relationship between permeability and stress:

$$k = k_0 \left[\log \left(\frac{\sigma}{\sigma_0} \right) \right]^3, \quad (5)$$

where σ_0 is the initial stress.

When rock is deforming plastically, the stress-loading path has a clear effect on the variation in permeability [25–28]. The primary factor influencing the variation in rock permeability under a complex loading path is not only porosity but also fracture size, density, and direction.

Bear [29] and Witherspoon et al. [30] successively derived the basic equations describing flow through a fracture. The simplest model of fracture flow is the well-known

cubic law [31]. Javadi et al. [32] proposed the cubic law relationship between fracture permeability and fracture characteristics.

$$k = \frac{w d^3}{12 A_f}, \quad (6)$$

where w is the fracture width, d is the aperture of the idealized parallel smooth fracture, and A_f is the cross-sectional area.

Relative displacement between fracture surfaces can induce changes in the volumetric strain. Several studies were conducted to determine the relationship between permeability and volumetric strain [28, 33, 34]. The relationship between the permeability and volumetric strain of fractured rock was given as follows [35]:

$$k = k_0 \exp \left\{ \frac{1}{K_p} \left[\frac{1 + \nu}{1 - \nu} (p - p_0) - \frac{2E}{3(1 - \nu)} (\varepsilon_V - \varepsilon_{V0}) \right] \right\}, \quad (7)$$

where the subscript 0 indicates initial values, K_p is the pore volume modulus, p is the fluid pressure in the fracture network, E is Young's modulus, ν is Poisson's ratio, and ε_V is the volumetric strain.

However, a rock sample undergoing plastic deformation is subjected to not only volumetric deformation but also shear deformation. Shear strain has an important and significant effect on permeability. In this paper, we report the results of conventional triaxial compression tests and fluid flow tests on sandstone samples using an MTS 816.02 rock-mechanics test system with a self-designed permeation system. These tests were conducted to investigate the permeability evolution law under complex loading path. Our aim was to explore the influence of plastic flow on the variation in permeability, based on the Mohr-Coulomb yield criterion and a nonassociated flow rule. This study proposes a new permeability prediction model that correlates the volumetric strain and the shear strain. The model was verified by comparing the predicted and experimental values of permeability.

2. Theoretical Principles

The relationship between permeability increments and stress increments can be established based on the strain increment-stress increment relationship and the permeability increment-strain increment relationship. In the following text, we briefly introduce the theory of plastic flow in rocks and the permeability prediction model.

2.1. Elasto-Plastic Constitutive Model of Rocks under Triaxial Compression. Axial strain ε_1 , radial strain ε_2 , and circumferential strain ε_3 occur in a rock sample under axial stress σ_1 , intermediate stress σ_2 , and confining stress σ_3 . Due to axis symmetry, it holds that $\sigma_3 = \sigma_2$, and $\varepsilon_3 = \varepsilon_2$. In the elastic

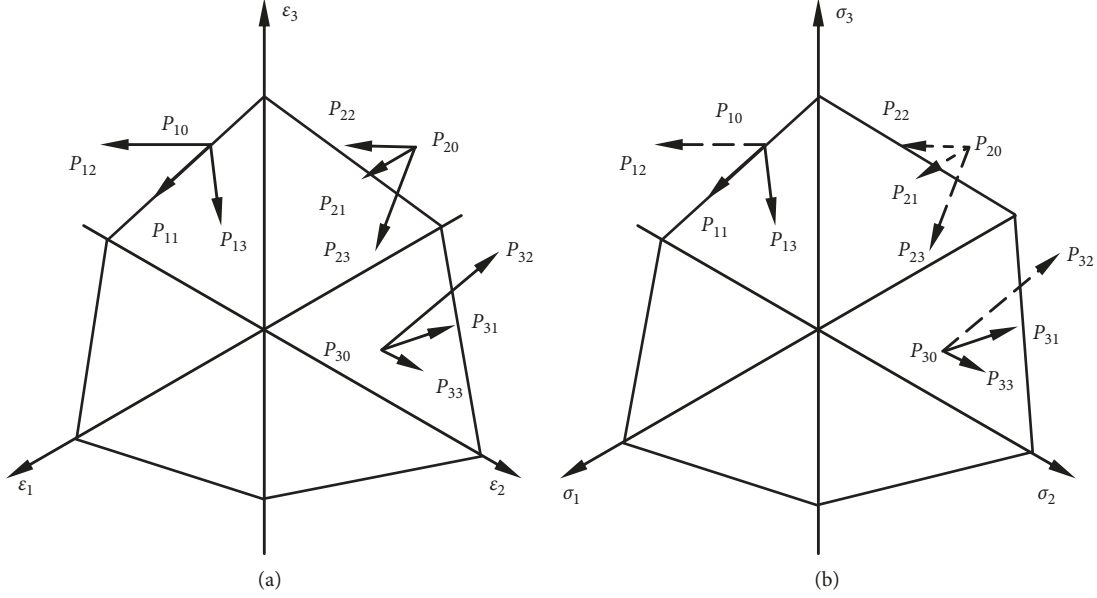


FIGURE 1: Flow paths on the deviatoric plane. (a) Principal strain space and (b) principal stress space.

deformation, the stress and strain components of a rock sample follow the generalized Hooke's law [36], i.e.,

$$\begin{aligned}\sigma_1 &= \Lambda \varepsilon_V + 2G\varepsilon_1, \\ \sigma_3 &= \Lambda \varepsilon_V + 2G\varepsilon_3,\end{aligned}\quad (8)$$

where ε_V is the volumetric strain, $\varepsilon_V = \varepsilon_1 + 2\varepsilon_3$, and Λ and G are the Lamé coefficients $\Lambda = E\nu/(1+\nu)(1-2\nu)$, and $G = E/2(1+\nu)$, respectively.

Shear yielding in rock obeys the Mohr-Coulomb criterion. If the compressive stress is positive, the yield condition can be expressed as equation (9) if $\sigma_1 \leq \sigma_2 \leq \sigma_3$:

$$\sigma_1 - \sigma_3 \tan^2 \alpha + 2c \tan \alpha = 0, \quad (9)$$

where c is the cohesion of rock, α is the angle of shear failure, $\alpha = 90^\circ + \varphi/2$, and φ is the internal friction angle.

In the event that plastic flow occurs in the rock sample after yielding, the flow paths can be represented by a directed line segment on the deviatoric plane, as shown in Figure 1. In principal strain space, the flow paths can be categorized into nine cases, as shown in Figure 1(a): (1) flow from one point P_{10} on the yield surface to another point P_{11} on the yield surface ($P_{10} \rightarrow P_{11}$), (2) flow from one point P_{10} on the yield surface to one point P_{12} outside the yield surface ($P_{10} \rightarrow P_{12}$), (3) flow from one point P_{10} on the yield surface to one point P_{13} inside the yield surface ($P_{10} \rightarrow P_{13}$), (4) flow from one point P_{20} outside the yield surface to one point P_{21} on the yield surface ($P_{20} \rightarrow P_{21}$), (5) flow from one point P_{20} outside the yield surface to one point P_{22} outside the yield surface ($P_{20} \rightarrow P_{22}$), (6) flow from one point P_{20} outside the yield surface to one point P_{23} inside the yield surface ($P_{20} \rightarrow P_{23}$), (7) flow from one point P_{30} inside the yield surface to one point P_{31} on the yield surface ($P_{30} \rightarrow P_{31}$), (8) flow from one point P_{30} inside the yield

surface to one point P_{32} outside the yield surface ($P_{30} \rightarrow P_{32}$), and (9) flow from one point P_{30} inside the yield surface to another point P_{33} inside the yield surface ($P_{30} \rightarrow P_{33}$).

In principal stress space, the stress state must be located on the yield surface. Therefore, there are only four cases possible, with respect to plastic flow, on the deviatoric plane in principal stress space, as shown in Figure 1(b): (1) flow from one point P_{10} on the yield surface to another point P_{11} on the yield surface ($P_{10} \rightarrow P_{11}$), (2) flow from one point P_{10} on the yield surface to one point P_{13} inside the yield surface ($P_{10} \rightarrow P_{13}$), (3) flow from one point P_{30} inside the yield surface to one point P_{31} on the yield surface ($P_{30} \rightarrow P_{31}$), and (4) flow from one point P_{30} inside the yield surface to another point P_{33} inside the yield surface ($P_{30} \rightarrow P_{33}$). The dashed line in Figure 1(b) indicates impossible flow paths.

Plastic potential is related to not only the stress states but also the loading history. For rock, the plastic flow rule is nonassociated, and the plastic potential function can be described as a Mohr-Coulomb relationship, where c and φ are no longer constant but a function of the loading history. If the plastic internal variable χ is used to represent the loading history, the plastic potential function can be expressed as follows [37–40]:

$$\begin{aligned}F(\sigma_1, \sigma_3, \chi) &= \sigma_1 - \sigma_3 \tan^2 \left(45^\circ + \frac{\varphi(\chi)}{2} \right) \\ &\quad - 2c(\chi) \tan \left(45^\circ + \frac{\varphi(\chi)}{2} \right).\end{aligned}\quad (10)$$

Equation (10) is the plastic potential function with an isotropic hardening (softening) model, which is a group of potential functions that change in terms of $c(\chi)$ and $\varphi(\chi)$. χ is used to describe the plastic deformation history. The

plastic volumetric strain ε_V^p of rock can be selected as the internal variable:

$$\chi = \varepsilon_V^p = \varepsilon_1^p + 2\varepsilon_3^p, \quad (11)$$

When $\chi = 0$, we have $c(\chi)|_{\chi=0} = c$ and $\varphi(\chi)|_{\chi=0} = \varphi$, which correspond to equation (9). The values of $c(\chi)$ and $\varphi(\chi)$ can be obtained using a triaxial compression test.

Then, the flow rule is as follows:

$$\begin{aligned} \Delta\varepsilon_{1p} &= \Delta\lambda_s \frac{\partial F}{\partial \sigma_1} = \Delta\lambda_s, \\ \Delta\varepsilon_{3p} &= \Delta\lambda_s \frac{\partial F}{\partial \sigma_3} = -\Delta\lambda_s \tan^2\left(45^\circ + \frac{\varphi(\chi)}{2}\right), \end{aligned} \quad (12)$$

where $\Delta\varepsilon_{1p}$ and $\Delta\varepsilon_{3p}$ are the plastic strain increments and $\Delta\lambda_s$ is the plastic multiplier.

When the stress state induces flow on the yield surface, the plastic multiplier $\Delta\lambda_s$ can be expressed as follows:

$$\Delta\lambda_s = \frac{1}{\Lambda} \frac{F(\sigma_{1T}, \sigma_{3T})}{(1 - \nu/\nu) - 2 \tan^2\alpha - (1 - (1/\nu) \tan^2\alpha) \tan^2\alpha}, \quad (13)$$

where

$$\begin{aligned} \sigma_{1T} &= \sigma_1 + (\Lambda + 2G)\Delta\varepsilon_1 + 2\Lambda\Delta\varepsilon_3, \\ \sigma_{3T} &= \sigma_3 + 2\Lambda\Delta\varepsilon_1 + (\Lambda + 2G)\Delta\varepsilon_3. \end{aligned} \quad (14)$$

$$\Delta\lambda_s = \frac{1}{\Lambda} \frac{F(\sigma_{1T}, \sigma_{3T}) - F(\sigma_{1N}, \sigma_{3N})}{\Lambda(1 - \nu/\nu) - 2 \tan^2(45^\circ + (\varphi(\chi)/2)) - (1 - (1/\nu) \tan^2(45^\circ + (\varphi(\chi)/2))) \tan^2(45^\circ + (\varphi(\chi)/2))}. \quad (15)$$

Equation (15) shows the modified plastic flow rules for rock proposed in this paper.

2.2. Permeability Model for Plastic Flow. Assuming small deformation, the rock sample porosity ϕ is related to the rock volumetric strain as follows:

$$\phi = \phi_0 + \varepsilon_V, \quad (16)$$

where ϕ_0 is the initial porosity. Porosity is commonly measured by the mercury injection test.

The power-exponential relationship between the porosity and permeability of the rock samples in the post-peak region is given by [42]

$$k = k_0 \left(\frac{\phi}{\phi_0}\right)^{m_k}, \quad (17)$$

where m_k is the nondimensional coefficient.

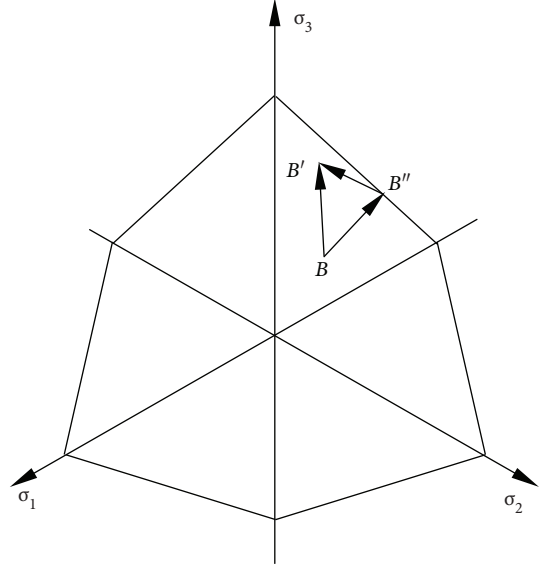


FIGURE 2: Flow paths inside the yield surface.

Equation (13) shows the plastic flow rules for geotechnical materials and is commonly used in geotechnical engineering [41].

When the stress state is inside the yield surface, the plastic multiplier $\Delta\lambda_s$ can no longer be calculated by equation (13). As shown in Figure 2, if the flow path of stress state is from B to B' ($B \rightarrow B'$), we can divide $B \rightarrow B'$ into $B \rightarrow B''$ and $B'' \rightarrow B'$ due to small deformation. The point B'' is on the yield surface. Therefore, we propose the following plastic multiplier expression according to equation (13):

Equation (18) can be written by taking the logarithm on both sides of equation (17):

$$\ln k = \ln k_0 + m_k \ln \left(\frac{\phi}{\phi_0}\right). \quad (18)$$

Equation (18) can be differentiated with respect to porosity ϕ to obtain

$$\frac{dk}{d\phi} = \frac{m_k}{\phi} k. \quad (19)$$

The permeability increment is easily obtained from equation (19):

$$\Delta k = \frac{m_k}{\phi} k \Delta\phi, \quad (20)$$

where $\Delta\phi$ is the porosity increment.

Equation (21) can be written by combining equations (16) and (19):

$$\Delta k = \frac{m_k}{\phi} k \Delta \varepsilon_V. \quad (21)$$

Equations (16) and (21) indicate that, in theory, only the volumetric strain changes the porosity and permeability, whereas the shear strain does not. However, the experimental results presented in this paper show that the shear deformation changes the permeability. To characterize the influence of the shear deformation on permeability, an equivalent shear strain is given by the following equation, according to the Mohr-Coulomb criterion:

$$\gamma_{MC} = \frac{2}{1-2\nu} (1-\nu \sec^2 \alpha) \varepsilon_1 + \frac{2}{1-2\nu} (2\nu - \tan^2 \alpha) \varepsilon_3. \quad (22)$$

Considering the influence of shear deformation, we have modified the equation to calculate permeability:

$$\Delta k = \frac{k}{\phi} \left(\lambda_1^k \Delta \varepsilon_V + \lambda_2^k \Delta \gamma_{MC} \right), \quad (23)$$

where λ_1^k and λ_2^k reflect the influence of the volumetric strain and equivalent shear strain, respectively, on the permeability. These parameters are defined as the permeability influence coefficients and can be estimated using the Monte Carlo method.

Equation (23) describes the changes in permeability due to plastic deformation and is known as the permeability model under plastic flow.

3. Experimental Samples, Principles, and Procedures

3.1. Experimental Samples. The standard cylindrical sandstone rock samples of 50 mm diameter and 100 mm length were cut from sandstone blocks that were collected from a coal mine in Shanxi Lu'an, China. To ensure the reliability of the experimental results, rock samples without obvious macroscopic cracks and joints were chosen. The two ends of the rock samples were polished to remove uneven surfaces [1]. Parts of sandstone samples are shown in Figure 3. The mineral composition of the sandstone is mainly quartz, feldspar, calcite, oxides, and mica, which is detected by the powder crystal X-ray diffraction testing machine. The initial porosity of the sandstone is 5.7%, and the order of magnitude of the initial permeability is 10^{-17} m^2 , which measured by a PoreMaster 33 mercury intrusion meter.

The triaxial compression tests were first performed to determine the sandstone sample mechanical parameters by using the MTS815.02 mechanics testing machine. The experiments were conducted under the confining pressure of 6.0 MPa. The values of the failure load, peak strength, peak strain, and elasticity modulus are shown in Table 1. The mean value and variable coefficient of peak strength are



FIGURE 3: Sandstone samples.

129.9 MPa and 4.30%, respectively. The mean value and variable coefficient of peak strain are 1.27% and 3.27%, respectively. The mean value and variable coefficient of the elasticity modulus are 9.64 GPa and 5.86%, respectively. The values of variable coefficient show that the dispersion of the sandstone samples is very small.

3.2. Experimental Principles

3.2.1. Triaxial Compression Test. In triaxial compression tests, the confining pressure remains constant. The sampling period in this study is $\tau = 1$ (s). The axial stress σ_1^i , the axial strain ε_1^i , and the circumferential strain ε_3^i of each rock sample are measured at the moment $t_i = (i-1)\tau$, where $i = 1, 2, \dots, N$.

We assume that the axial stress reaches a peak value σ_{1p} at the moment t_{N_p} ($N_p < N$), i.e., $\sigma_{1p} = \sigma_1^{N_p}$. For the elastic deformation, the relationship between stress and strain is described as follows:

$$\begin{aligned} \sigma_1^i &= \lambda \varepsilon_V^i + 2G\varepsilon_1^i, \\ \sigma_3^i &= \lambda \varepsilon_V^i + 2G\varepsilon_3^i, \end{aligned} \quad (24)$$

where ε_V^i is the volumetric strain of the rock samples at sampling time, and $\varepsilon_V^i = \varepsilon_1^i + 2\varepsilon_3^i$.

The strain of the rock sample can be divided into two parts, elastic strain and plastic strain, in which the elastic strain is given as follows:

$$\begin{aligned} \varepsilon_{1e}^i &= \frac{1}{E} (\sigma_1^i - 2\nu\sigma_3^i), \quad i = N_p + 1, N_p + 2, \dots, N, \\ \varepsilon_{3e}^i &= \frac{1}{E} (\sigma_3^i - 2\nu\sigma_1^i). \end{aligned} \quad (25)$$

Therefore, the plastic strain equation can be written as follows:

$$\begin{aligned} \varepsilon_{1p}^i &= \varepsilon_1^i - \varepsilon_{1e}^i, \quad i = N_p + 1, N_p + 2, \dots, N, \\ \varepsilon_{3p}^i &= \varepsilon_3^i - \varepsilon_{3e}^i, \end{aligned} \quad (26)$$

where the plastic internal variable is $\chi^i = \varepsilon_{Vp}^i = \varepsilon_{1p}^i + 2\varepsilon_{3p}^i$.

We conduct the triaxial compression tests at n_c different confining pressures, where σ_3^i ($i = 1, 2, \dots, n_c$). Then, n_c plastic

TABLE 1: Mechanical parameters of sandstone samples under the confining pressure of 6.0 MPa.

Serial no.	Dia. (mm)	Height (mm)	Confining pressure (MPa)	Failure load (kN)	Peak strength (MPa)	Peak strain (%)	Elasticity modulus (GPa)
1	49.8	99.7	6	246.1	125.4	1.24	9.21
2	50.1	100.2	6	244.3	124.5	1.23	9.08
3	49.7	100.1	6	267.5	136.3	1.33	10.35
4	49.6	99.4	6	250.8	127.8	1.25	9.45
5	50.1	99.7	6	265.7	135.4	1.29	10.13

internal variable axial stress ($\chi - \sigma_1$) curves can be obtained. To establish the relationship between $c(\chi)$, $\varphi(\chi)$, and χ , we set n_{vp} typical values of ${}^j\chi$ ($j=1, 2, \dots, n_{vp}$) and obtain the corresponding axial stress ${}^i\sigma_1$, where ($i=1, 2, \dots, n_c$, $j=1, 2, \dots, n_{vp}$), under ${}^i\sigma_3$ and ${}^j\chi$. Using equation (9), we can obtain the values of ${}^j c(\chi)$ and ${}^j \varphi(\chi)$ under different ${}^j\chi$ ($j=1, 2, \dots, n_{vp}$) by using linear regression.

3.2.2. Fluid Flow Test. In this study, we used a transient method to measure the permeability of a sandstone sample [1]. The principle of the method is shown in Figure 4.

The volume of storage tank 1 (ST1) is equal to the volume of storage tank 2 (ST2), and the pressures of the fluids in these tanks are p_1 and p_2 , respectively. The sandstone samples are standard cylindrical specimens of height H and cross-sectional area S . At the start of the test, the pressure at the ends of a sandstone sample are p_{10} and p_{20} ($p_{10} > p_{20}$). During the process of the permeability tests, the fluid from ST1 flows into ST2 through the rock sample. The pressure p_1 of the fluid in ST1 continuously decreases, while the pressure p_2 of the fluid in tank 2 continuously increases. The pressure gradient $p_2 - p_1/H$ gradually decreases until the two storage tank pressures reach equilibrium, as shown in Figure 5.

If the mass flow from ST1 into the rock sample is q and the rock sample is presaturated, then the mass flow from the rock sample into ST2 is also q . The flow velocity within the rock sample is $v = q/\rho S$, where ρ is the density of the fluid; due to the compressibility of the fluid, the following relationship can be obtained:

$$\frac{1}{c_f} = \rho \frac{dp_1}{d\rho}, \quad (27)$$

where c_f is the compressibility coefficient of the fluid.

Since $d\rho = -qdt/B$ and $q = \rho S v$, we arrive at the following expression:

$$\frac{dp_1}{dt} = -\frac{Sv}{c_f V}, \quad (28)$$

where V is the volume of the storage tank.



FIGURE 4: Principle of the transient method.

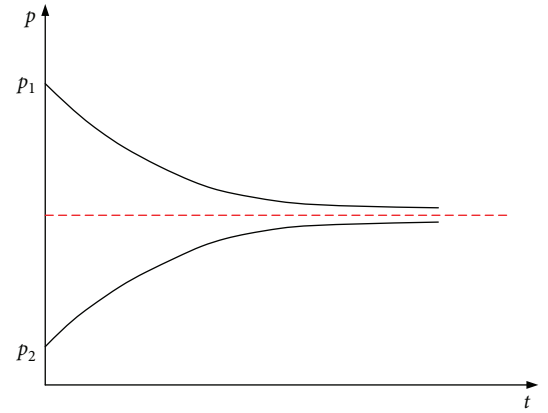


FIGURE 5: Variation curve of the storage tank pressure.

Similarly, we can write a similar expression for the other storage tank:

$$\frac{dp_2}{dt} = \frac{Sv}{c_f V}, \quad (29)$$

From equations (28) and (29), the expression for the flow velocity of the rock sample can be written as follows:

$$v = \frac{c_f V}{2S} \frac{d(p_1 - p_2)}{dt}. \quad (30)$$

According to Darcy's law, equation (30) is rewritten as follows:

$$v = -\frac{k}{\mu} \frac{p_2 - p_1}{H}, \quad (31)$$

where k is the permeability of the rock specimen and μ is the dynamic viscosity of the fluid.

Equation (32) can be derived by combining equations (30) and (31):

$$\frac{d(p_1 - p_2)}{p_1 - p_2} = -2 \frac{Sk}{c_f VH\mu} dt. \quad (32)$$

In the experiments, the sampling frequency is τ , the total number of measurements is n , and $t_f = n\tau$ can be calculated at the end of the sampling period. Equation (32) is integrated to obtain an equation in terms of the respective pressure values of the two storage tanks, p_{1f} and p_{2f} :

$$k = \frac{c_f VH\mu}{2t_f S} \ln \frac{p_{10} - p_{20}}{p_{1f} - p_{2f}}. \quad (33)$$

Deformation occurs when the rock sample is under considerable stress. The permeability variation is sensitive to the deformation of the rock samples. We test N stress states of the rock sample, i.e., $A_i(\sigma_1^{(i)}, \sigma_2^{(i)}, \sigma_3^{(i)})$, corresponding to N permeability values, i.e., $k^{(i)}$, $i = 1, 2, \dots, N$. A_M is the peak stress state, and A_1, A_2, \dots, A_{M-1} are the elastic deformation states, while $A_{M+1}, A_{M+2}, \dots, A_N$ are the plastic flow states.

The Lamé coefficients, Λ and G , for determining the elastic constitutive relations can be obtained by using the least-squares method, as described below.

The first step is to apply the generalized Hooke's law to define the relationship between the stress and strain components of A_1, A_2, \dots, A_{M-1} :

$$\begin{aligned} \sigma_1^{(i)} &= \Lambda \varepsilon_V^{(i)} + 2G\varepsilon_1^{(i)}, \quad i = 1, 2, \dots, M-1, \\ \sigma_3^{(i)} &= \Lambda \varepsilon_V^{(i)} + 2G\varepsilon_3^{(i)}. \end{aligned} \quad (34)$$

The second step is to construct a function based on the residual errors of equation (34):

$$\Pi = \sum_{i=1}^4 \left[\Lambda \varepsilon_V^{(i)} + 2G\varepsilon_1^{(i)} - \sigma_1^{(i)} \right]^2 + \sum_{i=1}^4 \left[\Lambda \varepsilon_V^{(i)} + 2G\varepsilon_3^{(i)} - \sigma_3^{(i)} \right]^2. \quad (35)$$

The third step is to define a system of linear equations related to Λ and G , which is based on the functional extremum conditions $\partial\Pi/\partial\Lambda = 0$ and $\partial\Pi/\partial G = 0$:

$$\begin{aligned} &\sum_{i=1}^4 \left(\Lambda \varepsilon_V^{(i)} \varepsilon_V^{(i)} + 2G\varepsilon_1^{(i)} \varepsilon_V^{(i)} - \sigma_1^{(i)} \varepsilon_V^{(i)} \right) \\ &+ \sum_{i=1}^4 \left(\Lambda \varepsilon_V^{(i)} \varepsilon_V^{(i)} + 2G\varepsilon_3^{(i)} \varepsilon_V^{(i)} - \sigma_3^{(i)} \varepsilon_V^{(i)} \right) = 0, \\ &\sum_{i=1}^4 \left(\Lambda \varepsilon_V^{(i)} \varepsilon_1^{(i)} + 2G\varepsilon_1^{(i)} \varepsilon_1^{(i)} - \sigma_1^{(i)} \varepsilon_1^{(i)} \right) \\ &+ \sum_{i=1}^4 \left(\Lambda \varepsilon_V^{(i)} \varepsilon_3^{(i)} + 2G\varepsilon_3^{(i)} \varepsilon_3^{(i)} - \sigma_3^{(i)} \varepsilon_3^{(i)} \right) = 0. \end{aligned} \quad (36)$$

The fourth step is to introduce the sign convention:

$$\begin{aligned} \begin{bmatrix} C_{11} & C_{12} \\ C_{21} & C_{22} \end{bmatrix} &= \begin{bmatrix} \sum_{i=1}^4 2\varepsilon_V^{(i)} \varepsilon_V^{(i)} & \sum_{i=1}^4 2\varepsilon_V^{(i)} (\varepsilon_1^{(i)} + \varepsilon_3^{(i)}) \\ \sum_{i=1}^4 \varepsilon_V^{(i)} (\varepsilon_1^{(i)} + \varepsilon_3^{(i)}) & \sum_{i=1}^4 2(\varepsilon_1^{(i)} \varepsilon_1^{(i)} + \varepsilon_3^{(i)} \varepsilon_3^{(i)}) \end{bmatrix}, \\ \begin{Bmatrix} B_1 \\ B_2 \end{Bmatrix} &= \begin{Bmatrix} \sum_{i=1}^4 \varepsilon_V^{(i)} (\sigma_1^{(i)} + \sigma_3^{(i)}) \\ \sum_{i=1}^4 (\sigma_1^{(i)} \varepsilon_1^{(i)} + \sigma_3^{(i)} \varepsilon_3^{(i)}) \end{Bmatrix}. \end{aligned} \quad (37)$$

The system of linear equations (36) of Λ and G are then transformed into a matrix:

$$\begin{bmatrix} C_{11} & C_{12} \\ C_{21} & C_{22} \end{bmatrix} \begin{Bmatrix} \Lambda \\ G \end{Bmatrix} = \begin{Bmatrix} B_1 \\ B_2 \end{Bmatrix}. \quad (38)$$

The last step is to obtain the optimal estimation of Λ and G by resolving the linear equation for the two unknowns.

The rock sample will yield at the point A_M where the principal stresses satisfy the Mohr-Coulomb criterion:

$$\sigma_1^{(M)} - \sigma_3^{(M)} \tan^2 \alpha + 2c \tan \alpha = 0. \quad (39)$$

From point A_M to point A_N , the rock sample is subjected to $N - M$ flow steps. Step 1 includes the flow from A_M to A_{M+1} , written as $A_M \rightarrow A_{M+1}$, and step 2 through steps $N - M$ are written as $A_{M+1} \rightarrow A_{M+2}$, $A_{M+2} \rightarrow A_{M+3}$, \dots , and $A_{N-1} \rightarrow A_N$, respectively.

According to equation (12), the plastic strain increment in the flow step $A_i \rightarrow A_{i+1}$ ($i = M, M+1, \dots, N-1$) is calculated as follows:

$$\begin{aligned} \Delta \varepsilon_{1p}^{(i)} &= \Delta \lambda_s^{(i)}, \quad i = M+1, M+2, \dots, N, \\ \Delta \varepsilon_{3p}^{(i)} &= -\Delta \lambda_s^{(i)} \tan^2 \left(45^\circ + \frac{\varphi(\chi)}{2} \right). \end{aligned} \quad (40)$$

The elastic strain increment is calculated as follows:

$$\begin{aligned} \Delta \varepsilon_{1e}^{(i)} &= \frac{1}{2G} \left[\Delta \sigma_1^{(i)} - \frac{\Lambda}{3\Lambda + 2G} (\Delta \sigma_1^{(i)} + 2\Delta \sigma_3^{(i)}) \right], \\ & \quad i = M+1, M+2, \dots, N, \\ \Delta \varepsilon_{3e}^{(i)} &= \frac{1}{2G} \left[\Delta \sigma_3^{(i)} - \frac{\Lambda}{3\Lambda + 2G} (\Delta \sigma_1^{(i)} + 2\Delta \sigma_3^{(i)}) \right]. \end{aligned} \quad (41)$$

Therefore, the strain components of the rock sample under the stress state A_{i+1} ($i = M, M + 1, \dots, N - 1$) are as follows:

$$\begin{aligned}\varepsilon_1^{(i)} &= \varepsilon_1^{(i-1)} + \Delta\varepsilon_{1e}^{(i)} + \Delta\varepsilon_{1p}^{(i)}, \quad i = M + 1, M + 2, \dots, N, \\ \varepsilon_3^{(i)} &= \varepsilon_3^{(i-1)} + \Delta\varepsilon_{3e}^{(i)} + \Delta\varepsilon_{3p}^{(i)}.\end{aligned}\quad (42)$$

Because stress state A_M is on the yield surface, the plastic multiplier in the flow step $A_M \rightarrow A_{M+1}$ is calculated according to equation (13):

$$\Delta\lambda_s^{(M+1)} = \frac{1}{\Lambda(1-\nu/\nu) - 2\tan^2\alpha - (1-(1/\nu)\tan^2\alpha)\tan^2\alpha} F(\sigma_{1T}^{(M+1)}, \sigma_{3T}^{(M+1)}), \quad (43)$$

$$\Delta\lambda_s^{(i)} = \frac{1}{\Lambda(1-\nu/\nu) - 2\tan^2(45^\circ + (\varphi(\chi)/2)) - (1-(1/\nu)\tan^2(45^\circ + (\varphi(\chi)/2)))\tan^2(45^\circ + (\varphi(\chi)/2))} F(\sigma_{1T}^{(i)}, \sigma_{3T}^{(i)}) - F(\sigma_{1T}^{(i-1)}, \sigma_{3T}^{(i-1)}), \quad i = M + 2, M + 3, \dots, N. \quad (45)$$

Equations (43) and (45) constitute the computational format of the plastic multiplier.

According to equations (40), (41), and (42), the computational format of the volumetric strain of the rock sample can be defined as follows:

$$\varepsilon_V^{(i)} = \varepsilon_V^{(i-1)} + \frac{[\sigma_m^{(i)} - \sigma_m^{(i-1)}]}{K} + \left(1 - 2\tan^2\left(45^\circ + \frac{\varphi(\chi)}{2}\right)\right)\Delta\lambda_s^{(i)}, \quad i = M + 1, M + 2, \dots, N, \quad (46)$$

where $\sigma_m^{(i)} = ((\sigma_1^{(i)} + 2\sigma_3^{(i)})/3)$ is the average principal stress.

The experimental values of permeability are recorded as k^i ($i = 1, 2, \dots, N$). The values of permeability after yielding can be calculated according to equations (17) and (23), and the iterative format is as follows:

$$\begin{aligned}k^{(M)} &= k_0 \left(\frac{\phi^{(M)}}{\phi_0}\right)^{m_k}, \\ \tilde{k}^{(i)} &= k^{(i-1)} + \frac{k^{(i-1)}}{\phi^{(i-1)}} \left(\lambda_1^k \Delta\varepsilon_V^{(i)} + \lambda_2^k \Delta\gamma_{MC}^{(i)}\right), \\ & i = M + 1, M + 2, \dots, N,\end{aligned}\quad (47)$$

where $\tilde{k}^{(i)}$ is the estimated value of permeability in the stress state A_i , $\Delta\varepsilon_V^{(i)} = \varepsilon_V^{(i)} - \varepsilon_V^{(i-1)}$ is the volumetric strain increment during plastic flow $A_i \rightarrow A_{i+1}$ ($i = M, M + 1, \dots, N - 1$), and

where

$$\begin{aligned}\sigma_{1T}^{(M+1)} &= \sigma_1^{(M)} + (\Lambda + 2G)\Delta\varepsilon_1^{(M+1)} + 2\Lambda\varepsilon_3^{(M+1)}, \\ \sigma_{3T}^{(M+1)} &= \sigma_3^{(M)} + 2\Lambda\Delta\varepsilon_1^{(M+1)} + (\Lambda + 2G)\Delta\varepsilon_3^{(M+1)}.\end{aligned}\quad (44)$$

Since the points $A_{M+1}, A_{M+2}, \dots, A_{N-1}$ are not on the yield surface, the plastic multipliers in the flow steps $A_{M+1} \rightarrow A_{M+2}, \dots$, and $A_{N-1} \rightarrow A_N$ are calculated according to equation (15):

$\Delta\gamma_{MC}^{(i)} = \gamma_{MC}^{(i)} - \gamma_{MC}^{(i-1)}$ is the equivalent shear strain increment during plastic flow $A_i \rightarrow A_{i+1}$ ($i = M, M + 1, \dots, N - 1$).

3.3. Experimental System. The experimental system includes an axial loading system, a confining pressure loop, a permeation loop, and a permeameter. The main functions performed by the system are as follows: (1) applying the axial loading to the rock sample, (2) applying the confining pressure to the rock sample, and (3) applying the pore pressure (seepage pressure) to the upper and lower ends of the rock sample. The rock sample was enclosed in the permeameter (Figure 6), and the MTS 816.02 rock mechanics testing system and TestStar II were used to apply an axial load to the permeameter, as shown in Figure 7. The permeameter is equipped with three nozzles: A, B, and C. Nozzle A is connected to the confining pressure loop, and nozzles B and C are connected to the permeation loop.

The permeameter is composed of a base plate (#1), lower steel plate (#2), porous disc (#3), cylindrical barrel (#4), upper steel plate (#5, #6), bleeder screw (#7, #8), piston (#1), cover plate (#12), and other components, as shown in Figure 6. There is a cavity between the rock sample and the cylindrical barrel, and the confining pressure system injects hydraulic oil into this cavity through nozzle A to apply the confining pressure (radial pressure) around the rock sample, as shown schematically in Figure 8. Nozzles B and C of the permeameter are connected to ST1 and ST2 in the permeation loop, respectively, and apply the pore pressure at both ends of the rock sample, as shown in Figure 9. The fluid in ST1 flows into the rock sample from nozzle B through the base plate, the lower steel plate, and the porous disc and flows into ST2 from nozzle C through another porous disc, the

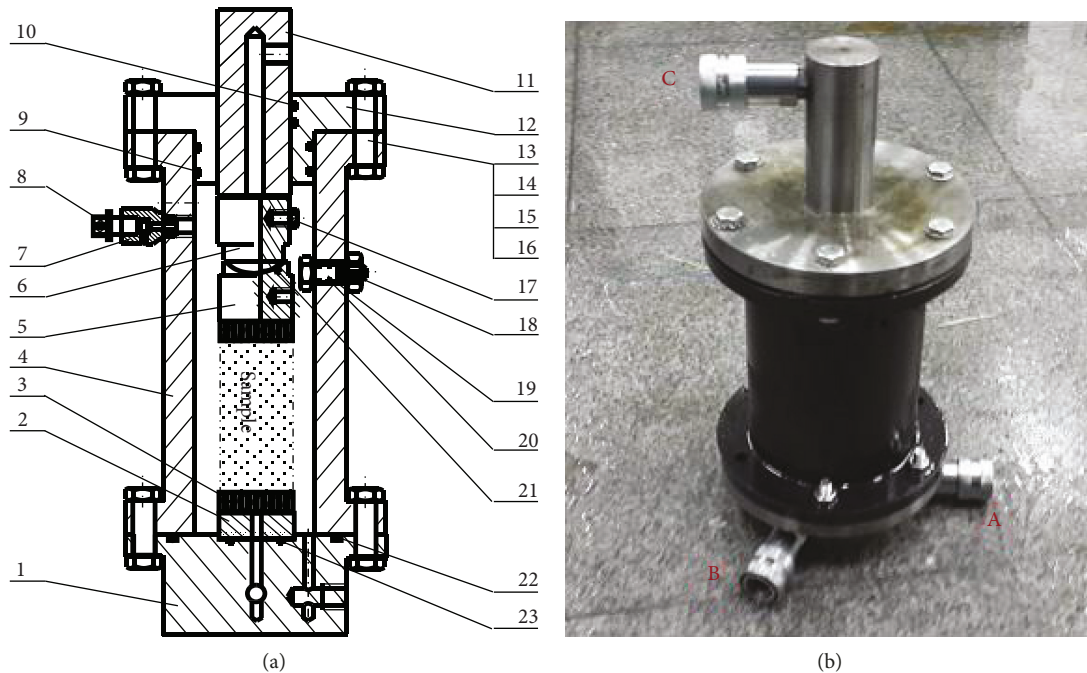


FIGURE 6: Permeameter: (a) schematic diagram and (b) photograph. (1) Base plate, (2) lower steel plate, (3) porous disc, (4) cylindrical barrel, (5) upper steel plate-concave surface, (6) upper steel plate-convex surface, (7) bleeder screw for the main body, (8) bleeder screw for the needle plug, (9-10) O-type rubber sealing ring, (11) piston, (12) cover plate, (13) bolt, (14) nut, (15) plain washer, (16) spring washer, (17) screw, (18) nut, (19) axis pin, and (20-23) O-type rubber sealing rings.



FIGURE 7: Connection between the permeameter and the MTS 816.02 rock mechanics testing system.

upper steel plate, and the piston. The cylindrical barrel is connected to the base plate and the cover plate by means of threaded fasteners (#13, #14, #15, and #16 in Figure 6). O-type rubber sealing rings are used to create seals

between the cylindrical barrel and the cover plate, between the cylindrical barrel and the base plate, and between the cover plate and the piston (#20, #21, #22, and #23 in Figure 6). The upper steel plates (#5 and #6 in Figure 6) use a spherical contact structure to uniformly distribute the axial force. The air in the confining pressure cavity is evacuated via the bleeder screw (#7 and #8 in Figure 6).

In the confining pressure system (see Figure 8), the valve spool of the directional control valve (DCV) is an M-type function valve. Before the fluid flow test, the spool is set to the left-hand position, and the hydraulic oil flows into the cavity via the plunger pump (PP) through both the DCV valve and the combined valve (a one-way valve and a throttle valve). At this point of the experiment, the one-way valve is not operational; the flow rate is adjusted by turning the hand wheel of the throttle valve (TV), and the confining pressure is adjusted by turning the hand wheel of the relief valve (RV). In the fluid flow test process, the confining pressure remains constant. After the test is completed, with the RV in the neutral position, the hydraulic oil flows directly to the oil tank (OT) through the PP. When the rock sample is removed, the cut-off valve (COV) is opened, and the RV will be placed in the right-hand position. At this point, the one-way valve in the combined valve is operational. The hydraulic oil in the cavity then flows back to the OT through the one-way valve and the COV.

In the permeameter loop, the volume of the storage tanks is an index of the permeability measurement ranges. Before the fluid flow test, the pressure values of ST1 and ST2 are set to p_{10} and p_{20} . The process to set the initial storage tank

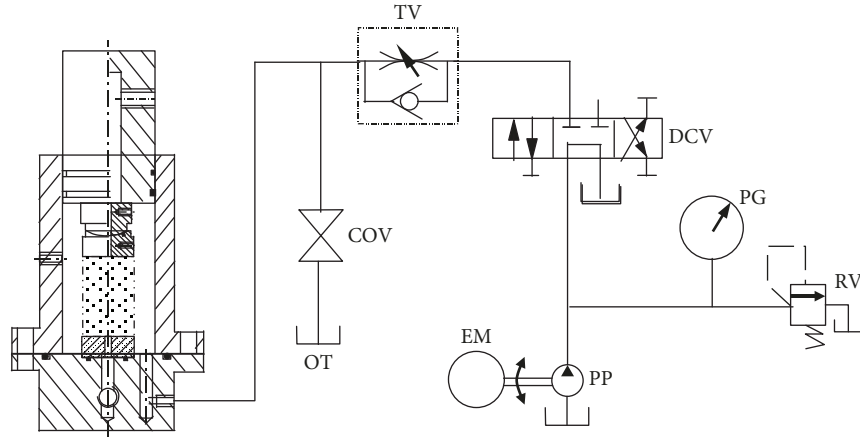


FIGURE 8: Schematic of the confining pressure system.

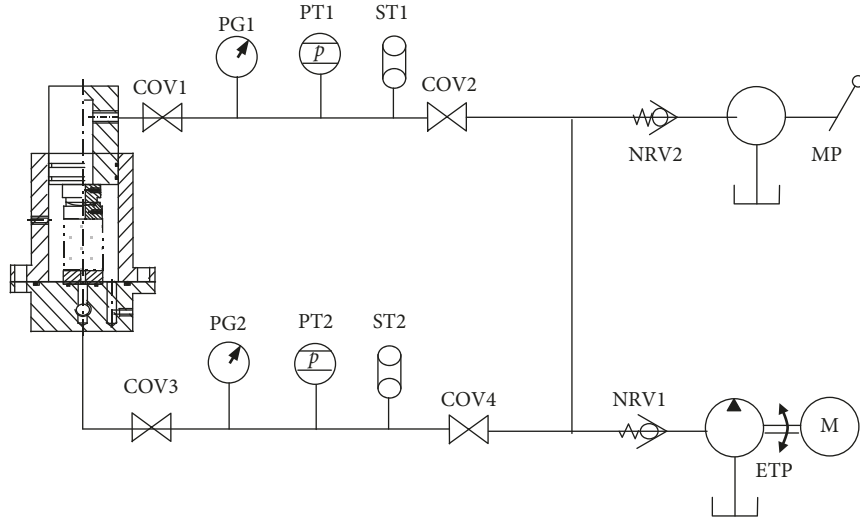


FIGURE 9: Schematic of the permeation loop.

pressures is as follows: turn on COV1, COV2, COV3, and COV4; start the electric test pump so that the pressure of the entire loop stabilizes to p_{20} ; turn off COV1, COV3, and COV4; pressurize the pipeline with the manual pump (MP); finally, stop the MP and turn off COV2 when the pressure of ST1 is stabilized at p_{10} . During the test, COV1 and COV3 are turned on at the same time, and the pressure in the two tanks is recorded. After the test, COV1, COV2, COV3, and COV4 are turned on at the same time.

3.4. Experimental Procedure. Before the fluid flow test, the rock specimens were saturated with water. The test was divided into 11 steps, corresponding to the 11 stress states $A_i(\sigma_1^{(i)}, \sigma_2^{(i)}, \sigma_3^{(i)})$ and 11 strain states $A_i(\epsilon_1^{(i)}, \epsilon_2^{(i)}, \epsilon_3^{(i)})$, ($\sigma_2^{(i)} = \sigma_3^{(i)}$, and $\epsilon_2^{(i)} = \epsilon_3^{(i)}$, $i = 1, 2, \dots, 11$). The displacement controlling method is used in the test with constant strain rate of $2 \times 10^{-5} \text{ s}^{-1}$. Each step of the fluid flow test had a sampling time of 1000 s, with a sampling rate of 1 Hz. The flow chart of the procedure for the fluid flow test is shown in Figure 10.

4. Experimental Results

4.1. Triaxial Compression Test Results. We conducted a series of conventional triaxial compression tests under confining pressures of 2 MPa, 4 MPa, 6 MPa, 8 MPa, and 10 MPa. The test results are presented in Table 2.

The plastic volumetric strain of rock samples R-TS1, R-TS4, R-TS8, R-TS12, and R-TS15 was calculated according to the method described in Section 3.1. Then, we obtained 5 plastic internal variable versus axial stress curves, one for each of the confining pressures tested, as shown in Figure 11.

We calculated the values of $c(\chi)$ and $\phi(\chi)$ corresponding to the plastic volume strains of 0.0, 0.001, 0.002, 0.003, 0.004, and 0.005 by using equation (10), and the results are presented in Figure 12 and Table 3.

4.2. Fluid Flow Test Results and Analysis. The fluid flow tests were carried out under $N = 11$ stress states, specifically $A_i (i = 1, 2, \dots, 11)$. Each of the rock samples had a diameter of 49.6 mm and a height of 99.2 mm. Water was used as the flow liquid; the water had a mass density of $\rho = 1000 \text{ kg/m}^3$,

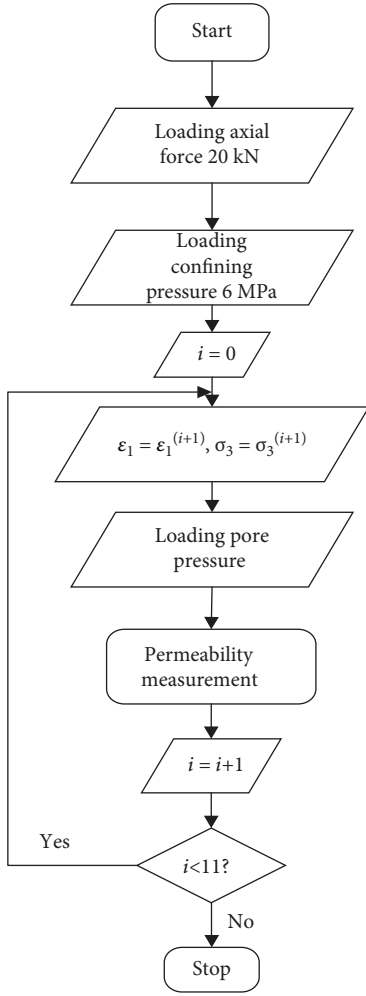


FIGURE 10: Flow chart of the fluid flow test with triaxial compression.

dynamic viscosity of $\mu = 1.002 \times 10^{-3} \text{ Pa} \cdot \text{s}$ at 20°C , and a compressibility coefficient of $c_f = 0.458 \times 10^{-9} \text{ Pa}^{-1}$.

At the start of the fluid flow test, the pressures at the ends of the sandstone sample are $p_{10} = 5 \text{ MPa}$ and $p_{20} = 3 \text{ MPa}$; therefore, the pore pressure difference is 2 MPa . In the pre-peak strength state, the confining pressure is set as 6 MPa . To investigate the influence of plastic flow on the permeability of the sandstone, the axial stress and confining pressure of the rock samples were both changed after the seventh step of the permeability test.

The axial stress-strain curve of the sandstone sample is shown in Figure 13. As seen in Figure 13, the axial stress reaches a peak value at point A_5 . At that point, the rock sample is considered to be deforming via shear yielding. Therefore, points A_1, \dots, A_4 describe the pre-peak strength state, and points A_6, \dots, A_{11} describe the plastic flow state. The rock sample went through a 6-step plastic flow, represented by points $A_5 - A_{11}$ in Figure 13. The values of the axial stress σ_1 , confining pressure σ_3 , axial strain ε_1 , and circumferential strain ε_3 measured during the test are presented in Table 4. The sign convention of ε_1 , ε_3 , and ε_V is that ε_1 and ε_3 in compression are positive and ε_V in dilation is positive.

For $A_i (i = 1, \dots, 4)$, in the elastic deformation state, the values of the Lamé coefficients Λ and G of the sandstone sample were obtained according to the method described from equation (34) to equation (38), where

$$\begin{bmatrix} C_{11} & C_{12} \\ C_{21} & C_{22} \end{bmatrix} = \begin{bmatrix} 2.42 \times 10^{-4} & 2.85 \times 10^{-4} \\ 1.42 \times 10^{-4} & 4.62 \times 10^{-4} \end{bmatrix} \quad (48)$$

$$\text{and } \begin{Bmatrix} B_1 \\ B_2 \end{Bmatrix} = \begin{Bmatrix} 1.74 \times 10^6 \\ 2.13 \times 10^6 \end{Bmatrix}.$$

Then, the values of the Lamé coefficients are $\Lambda = 2.75$ (GPa) and $G = 3.76$ (GPa).

A total of 6 plastic flow steps occurred after yielding of the rock sample, $A_i \rightarrow A_{i+1}$ ($i = 5, \dots, 10$). The values of the stress increments ($\Delta\sigma_1$ and $\Delta\sigma_3$), strain increments ($\Delta\varepsilon_1$ and $\Delta\varepsilon_3$), plastic potential increment ($\Delta F = (\partial F/\partial\sigma_1)\Delta\sigma_1 + (\partial F/\partial\sigma_3)\Delta\sigma_3$), and plastic multiplier $\Delta\lambda_s^{(i)}$ ($i = 6, \dots, 11$) in each flow step are presented in Table 5.

As shown in Table 5, the flow steps $A_5 \rightarrow A_6$, $A_6 \rightarrow A_7$, $A_8 \rightarrow A_9$, and $A_{10} \rightarrow A_{11}$ show the unloading process, and $A_7 \rightarrow A_8$ and $A_9 \rightarrow A_{10}$ show the loading process. The plastic multiplier lies between -4.7×10^{-4} and 6.79×10^{-3} , and it is positive during the unloading steps ($\Delta F < 0$) and negative during the loading steps.

The volumetric strain, porosity, equivalent shear strain, and permeability of each stress state after the sample yielded $A_i (i = 6, 7, \dots, 11)$ are presented in Table 6.

As seen in Table 7, the volumetric strain increments during the first unloading process $A_5 \rightarrow A_6$ and $A_8 \rightarrow A_9$ are positive, and the volumetric strain increments during the later unloading processes $A_6 \rightarrow A_7$ and $A_{10} \rightarrow A_{11}$ are negative. In addition, the volumetric strain increment during the loading process $A_7 \rightarrow A_8$ is negative, and the volumetric strain increment during the loading process $A_9 \rightarrow A_{10}$ is zero. These changes in the sign of the volumetric strain increment indicate that there is no one-to-one relationship between the volumetric strain/variation and either loading or unloading. Similarly, there is also no one-to-one relationship between the equivalent shear strain variation and either loading or unloading.

Shear deformation occurred in the rock sample during the loading steps of $A_9 \rightarrow A_{10}$, without volume deformation. A permeability increment magnitude on the order of 1×10^{-20} was observed at this step, and a permeability increment magnitude on the order of 1×10^{-17} to 1×10^{-18} was observed during the other steps. Therefore, the influence of the shear strain on permeability is less than that of the volumetric strain.

The region of search for λ_1^k was $[2, 3]$, and the region of search for λ_2^k was $[0.01, 0.5]$. By using the Monte Carlo method, the optimal estimated values of the permeability influence coefficients were obtained as $\lambda_1^k = 2.55$ and $\lambda_2^k = 0.102$. We found that $\lambda_2^k < \lambda_1^k$, which proves that the influence of the shear strain on permeability is less than that of the volumetric strain.

TABLE 2: Triaxial compressive strength of the sandstone samples.

No.	Serial no.	Dia. (mm)	Height (mm)	Confining pressure (MPa)	Failure load (kN)	Compressive strength (MPa)
1	R-TS1	50.1	99.9		174.07	88.7
2	R-TS2	50.3	99.3	2.0	171.52	87.4
3	R-TS3	49.9	100.1		177.21	90.3
4	R-TS4	49.6	99.6		233.93	119.2
5	R-TS5	49.5	99.4	4.0	230.40	117.4
6	R-TS6	50.1	100.3		236.48	120.5
7	R-TS7	49.7	99.3		268.67	136.9
8	R-TS8	49.2	100.4	6.0	262.39	133.7
9	R-TS9	50.1	99.2		256.30	130.6
10	R-TS10	49.7	99.6		281.03	143.2
11	R-TS11	50.2	100.2	8.0	288.68	147.1
12	R-TS12	49.6	99.4		283.58	144.5
13	R-TS13	50.4	100.2		299.48	152.6
14	R-TS14	50.3	99.8	10.0	315.37	160.7
15	R-TS15	50.1	100.4		304.97	155.4

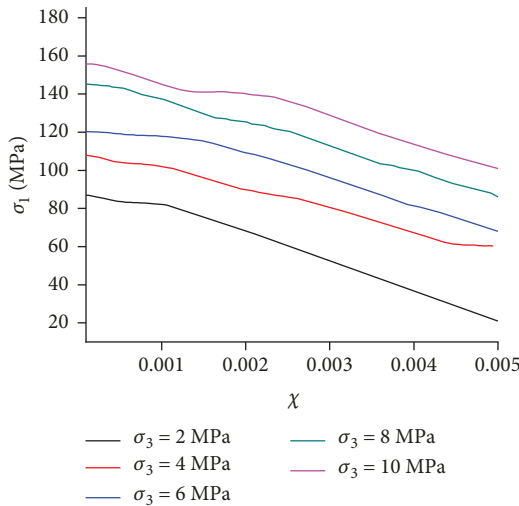
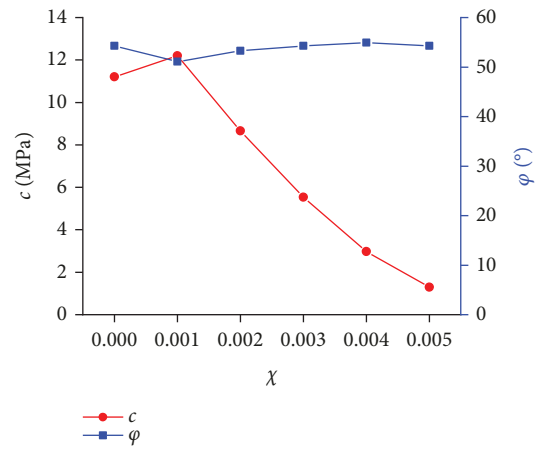


FIGURE 11: Plastic internal variable versus axial stress curves under various confining pressures.

From the fluid flow test results and the calculated values of λ_1^k and λ_2^k , it can be concluded that both shear strain and volumetric strain have an obvious effect on permeability. These two results both verify that the volumetric strain has a major effect on permeability.

The estimated values of permeability under every stress state after shear yielding, calculated by using equation (47), are presented in Figure 14 and Table 8.

Table 8 shows that the error between the estimated values and the experimental values in the stress state A_6 is 16.5%, which is because the axial stress decreases sharply as soon as the rock sample reaches the peak stress state. The errors in the stress states A_7, \dots, A_{11} were between 0.22% and

FIGURE 12: The change in c and φ with χ .TABLE 3: The calculated results of $c(\chi)$ and $\varphi(\chi)$ with varying χ .

χ	$c(\chi)$	$\varphi(\chi)$
0	11.2	54.3
0.001	12.2	51.1
0.002	8.66	53.3
0.003	5.53	54.3
0.004	2.98	54.9
0.005	1.29	54.3

1.20%. These small errors indicate that the iterative format for estimating permeability, represented by equation (47), is generally stable.

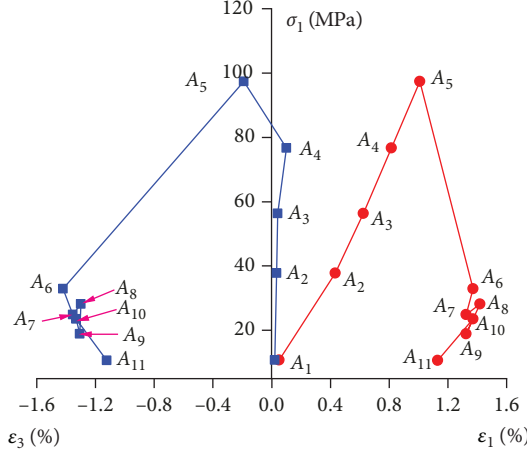


FIGURE 13: Relationship obtained between the axial stress and strain of the sandstone sample.

TABLE 4: Axial stress, confining pressure, axial strain, and circumferential strain.

State	σ_1 (MPa)	σ_3 (MPa)	ϵ_1 (%)	ϵ_3 (%)	State
A ₁	10.75	6	0.051	0.022	Pre-peak
A ₂	37.78	6	0.434	0.033	Pre-peak
A ₃	56.29	6	0.625	0.040	Pre-peak
A ₄	76.68	6	0.816	0.100	Pre-peak
A ₅	97.43	6	1.008	-0.189	Shear yielding
A ₆	32.92	6	1.372	-1.421	Plastic flow
A ₇	24.95	7.25	1.324	-1.353	Plastic flow
A ₈	28.19	5	1.419	-1.300	Plastic flow
A ₉	18.87	5.66	1.324	-1.307	Plastic flow
A ₁₀	23.51	5.9	1.372	-1.332	Plastic flow
A ₁₁	10.7	5.9	1.132	-1.123	Plastic flow

5. Discussion

In this study, we conducted fluid flow tests under 11 stress states. The permeability variation law for the sandstone samples after shear yielding was discussed. The strain increments after yielding included both the elastic strain increments and plastic strain increments. The former is directly given according to the generalized Hooke's law, while the latter is given by the flow rule, and the total strain increments are as follows:

$$\begin{aligned}\Delta\epsilon_1 &= \frac{1}{2G} \left[\Delta\sigma_1 - \frac{\Lambda}{3\Lambda+2G} (\Delta\sigma_1 + 2\Delta\sigma_3) \right] + \Delta\lambda_s, \\ \Delta\epsilon_3 &= \frac{1}{2G} \left[\Delta\sigma_3 - \frac{\Lambda}{3\Lambda+2G} (\Delta\sigma_1 + 2\Delta\sigma_3) \right] \\ &\quad - \Delta\lambda_s \tan^2 \left(45^\circ + \frac{\varphi(\chi)}{2} \right).\end{aligned}\quad (49)$$

According to equations (22) and (49), the volumetric strain increment $\Delta\epsilon_V$ and the equivalent strain increment $\Delta\gamma_{MC}$ can be written as follows:

$$\begin{aligned}\Delta\epsilon_V &= \frac{1}{2G} \left[\Delta\sigma_1 - \frac{\Lambda}{3\Lambda+2G} (\Delta\sigma_1 + 2\Delta\sigma_3) \right] + \Delta\lambda_s \\ &\quad + \frac{1}{G} \left[\Delta\sigma_3 - \frac{\Lambda}{3\Lambda+2G} (\Delta\sigma_1 + 2\Delta\sigma_3) \right] \\ &\quad - 2\Delta\lambda_s \tan^2 \left(45^\circ + \frac{\varphi(\chi)}{2} \right),\end{aligned}\quad (50)$$

$$\begin{aligned}\Delta\gamma_{MC} &= \frac{2}{1-2\nu} \left[1 - \nu \sec^2 \left(45^\circ + \frac{\varphi(\chi)}{2} \right) \right] \\ &\quad \cdot \left\{ \frac{1}{2G} \left[\Delta\sigma_1^{(i)} - \frac{\Lambda}{3\Lambda+2G} (\Delta\sigma_1^{(i)} + 2\Delta\sigma_3^{(i)}) \right] + \Delta\lambda_s \right\} \\ &\quad + \frac{2}{1-2\nu} \left[2\nu - \tan^2 \left(45^\circ + \frac{\varphi(\chi)}{2} \right) \right] \\ &\quad \cdot \left\{ \frac{1}{2G} \left[\Delta\sigma_3^{(i)} - \frac{\Lambda}{3\Lambda+2G} (\Delta\sigma_1^{(i)} + 2\Delta\sigma_3^{(i)}) \right] \right. \\ &\quad \left. - \Delta\lambda_s \tan^2 \left(45^\circ + \frac{\varphi(\chi)}{2} \right) \right\}.\end{aligned}\quad (51)$$

The expression between the permeability increment and the stress increment in plastic flow can be obtained by substituting equations (50) and (51) into equation (23):

$$\begin{aligned}\Delta k &= \frac{k}{\phi} \lambda_1^k \left\{ \frac{1}{2G} \left[\Delta\sigma_1 - \frac{\Lambda}{3\Lambda+2G} (\Delta\sigma_1 + 2\Delta\sigma_3) \right] + \Delta\lambda_s \right. \\ &\quad \left. + \frac{1}{G} \left[\Delta\sigma_3 - \frac{\Lambda}{3\Lambda+2G} (\Delta\sigma_1 + 2\Delta\sigma_3) \right] \right. \\ &\quad \left. - 2\Delta\lambda_s \tan^2 \left(45^\circ + \frac{\varphi(\chi)}{2} \right) \right\} \\ &\quad + \frac{k}{\phi} \lambda_2^k \left\{ \frac{2}{1-2\nu} \left(1 - \nu \sec^2 \left(45^\circ + \frac{\varphi(\chi)}{2} \right) \right) \right. \\ &\quad \left. \cdot \left[\frac{1}{2G} \left(\Delta\sigma_1 - \frac{\Lambda}{3\Lambda+2G} (\Delta\sigma_1 + 2\Delta\sigma_3) \right) + \Delta\lambda_s \right] \right. \\ &\quad \left. + \frac{2}{1-2\nu} \left(2\nu - \tan^2 \left(45^\circ + \frac{\varphi(\chi)}{2} \right) \right) \right. \\ &\quad \left. \cdot \left[\frac{1}{2G} \left(\Delta\sigma_3^{(i)} - \frac{\Lambda}{3\Lambda+2G} (\Delta\sigma_1 + 2\Delta\sigma_3) \right) \right. \right. \\ &\quad \left. \left. - \Delta\lambda_s \tan^2 \left(45^\circ + \frac{\varphi(\chi)}{2} \right) \right] \right\}.\end{aligned}\quad (52)$$

Based on equation (52), an iterative format is constructed to estimate the permeability increment in each step and the permeability at each stress-strain state, after shear yielding.

The performances of the plastic flow rule and the permeability model are discussed below.

TABLE 5: Stress increment and strain increment during plastic flow of the rock sample.

Step	$\Delta\sigma_1$ (MPa)	$\Delta\sigma_3$ (MPa)	$\Delta\varepsilon_1$ (%)	$\Delta\varepsilon_3$ (%)	$\Delta\lambda_s$	ΔF	State
$A_5 \rightarrow A_6$	-64.5	0	0.364	-1.23	$6.79E-3$	-64.50	Unloading
$A_6 \rightarrow A_7$	-7.97	1.25	-0.048	0.068	$9.02E-4$	-15.63	Unloading
$A_7 \rightarrow A_8$	3.24	-2.25	0.095	0.053	$-4.55E-4$	17.03	Loading
$A_8 \rightarrow A_9$	-9.32	0.66	-0.095	-0.007	$1.01E-3$	-13.37	Unloading
$A_9 \rightarrow A_{10}$	4.64	0.24	0.048	-0.025	$-4.75E-4$	3.17	Loading
$A_{10} \rightarrow A_{11}$	-12.8	0	-0.24	0.209	$1.35E-3$	-12.80	Unloading

TABLE 6: Volumetric strain, porosity, equivalent shear strain, and permeability of each stress state.

State	ε_v (%)	ϕ (%)	γ_{MC} (%)	$k(m^{-2})$
A_6	1.47	7.50	6.03	9.28×10^{-17}
A_7	1.38	7.23	5.77	9.00×10^{-17}
A_8	1.18	6.88	5.83	8.37×10^{-17}
A_9	1.29	6.99	5.66	8.71×10^{-17}
A_{10}	1.29	7.20	5.81	8.72×10^{-17}
A_{11}	1.11	6.81	4.86	8.17×10^{-17}

TABLE 7: Strain increment and permeability increment during plastic flow of the rock sample.

Step	$\Delta\varepsilon_v$ (%)	$\Delta\gamma_{MC}$ (%)	$\Delta k(m^{-2})$	State
$A_5 \rightarrow A_6$	2.10	3.66	5.38×10^{-17}	Unloading
$A_6 \rightarrow A_7$	-0.27	-0.25	-2.7×10^{-18}	Unloading
$A_7 \rightarrow A_8$	-0.20	0.05	-6.28×10^{-18}	Loading
$A_8 \rightarrow A_9$	0.11	-0.16	3.38×10^{-18}	Unloading
$A_9 \rightarrow A_{10}$	0.00	0.15	6.00×10^{-20}	Loading
$A_{10} \rightarrow A_{11}$	-0.18	-0.96	-5.49×10^{-18}	Unloading

5.1. *Plastic Flow Rule.* Substituting equations (40) and (41) into equation (42), we obtain the following equation:

$$\begin{cases} \varepsilon_1^{(i)} = \varepsilon_1^{(i-1)} + \frac{1}{2G} \left[\Delta\sigma_1^{(i)} - \frac{\Lambda}{3\Lambda+2G} (\Delta\sigma_1^{(i)} + 2\Delta\sigma_3^{(i)}) \right] + \lambda_s^{(i)} \\ \varepsilon_3^{(i)} = \varepsilon_3^{(i-1)} + \frac{1}{2G} \left[\Delta\sigma_3^{(i)} - \frac{\Lambda}{3\Lambda+2G} (\Delta\sigma_1^{(i)} + 2\Delta\sigma_3^{(i)}) \right] - \lambda_s^{(i)} \tan^2 \left(45^\circ + \frac{\varphi}{2} \right) \end{cases}, \quad (53)$$

where $\Delta\sigma_1^{(i)} = \sigma_1^{(i)} - \sigma_1^{(i-1)}$ and $\Delta\sigma_3^{(i)} = \sigma_3^{(i)} - \sigma_3^{(i-1)}$ for $i = 6, 7, \dots, 11$.

The flow rule represented by equation (53) is a mapping of $R^2 \rightarrow R^2$; however, geometrically comparing the estimated value of the strain component with the experimental value is difficult. Therefore, we introduce the equivalent shear stress that corresponds to the Mohr-Coulomb yield criterion:

$$\tau_{MC} = \sigma_1 - \sigma_3 \tan^2 \left(45^\circ + \frac{\varphi(\chi)}{2} \right). \quad (54)$$

Before yielding, the equivalent shear stress τ_{MC} is linearly related to the equivalent shear strain γ_{MC} , i.e., $\tau_{MC} = G\gamma_{MC}$. After yielding, $\tau_{MC} \leq 2c \tan \alpha$ and $\tau_{MC} \neq G\gamma_{MC}$.

The equivalent shear stress $\tau_{MC}^{(i)}$ and the equivalent shear strain $\gamma_{MC}^{(i)}$, where $(i = 6, 7, \dots, 11)$ are calculated for each stress state according to equations (54) and

(22). The increment of equivalent shear strain is found to be $\Delta\gamma_{MC}^{(i)} = \gamma_{MC}^{(i)} - \gamma_{MC}^{(i-1)}$ by combining equations (22) and (54), where $(i = 6, 7, \dots, 11)$, and the estimated value of the equivalent shear strain is $\tilde{\gamma}_{MC}^{(i)} = \tilde{\gamma}_{MC}^{(i-1)} + \Delta\gamma_{MC}^{(i)}$, where $(i = 6, 7, \dots, 11)$; these values are also calculated for each stress state.

Figure 15 shows the estimated values and experimental values of the equivalent shear strain corresponding to the equivalent shear stress $\tau_{MC}^{(i)}$, where $(i = 6, 7, \dots, 11)$. Figure 15 shows that the estimated equivalent shear strain values are approximately equal to the experimental values in each state after yielding. It can be argued that the flow rule estimation of the equivalent shear strain, as proposed in this paper, is highly accurate.

5.2. *Permeability Model.* The permeability model represented by equation (47) estimates the permeability \tilde{k}^i at the A_i state, based on the experimental value of permeability

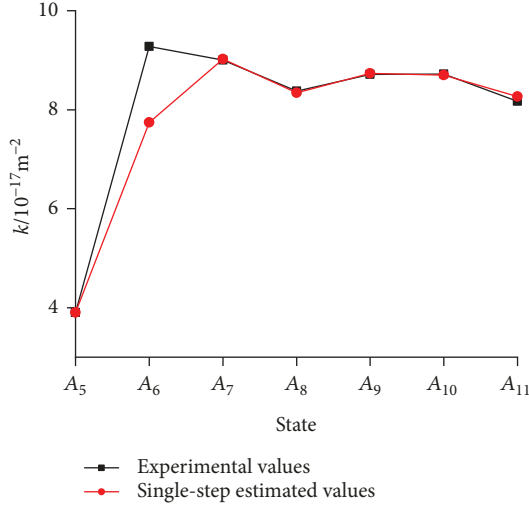


FIGURE 14: Single-step estimation of the permeability after shear yielding.

TABLE 8: Experimental values, estimated values, and relative errors of the permeability.

State	Permeability (m ⁻²)		
	Experimental values	Single-step estimated values	Relative error (%)
A ₅	3.90 × 10 ⁻¹⁷	3.90 × 10 ⁻¹⁷	—
A ₆	9.28 × 10 ⁻¹⁷	7.75 × 10 ⁻¹⁷	16.5%
A ₇	9.00 × 10 ⁻¹⁷	9.03 × 10 ⁻¹⁷	0.28%
A ₈	8.37 × 10 ⁻¹⁷	8.34 × 10 ⁻¹⁷	0.41%
A ₉	8.71 × 10 ⁻¹⁷	8.73 × 10 ⁻¹⁷	0.26%
A ₁₀	8.72 × 10 ⁻¹⁷	8.70 × 10 ⁻¹⁷	0.22%
A ₁₁	8.17 × 10 ⁻¹⁷	8.27 × 10 ⁻¹⁷	1.20%

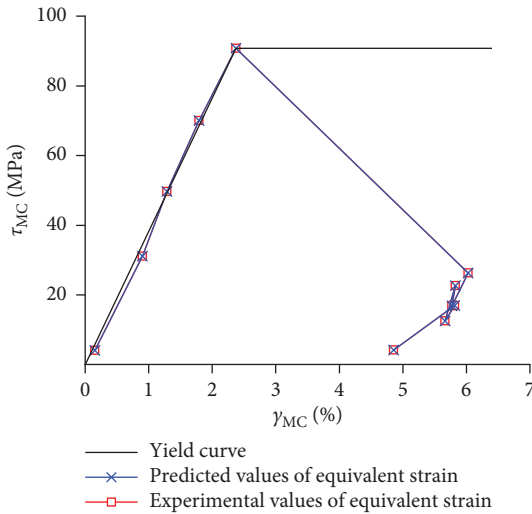


FIGURE 15: Estimated result of the equivalent shear stress and shear strain.

TABLE 9: Multistep permeability estimation.

State	Permeability (m ⁻²)		
	Experimental values	Multistep estimated values	Relative error (%)
A ₅	3.90 × 10 ⁻¹⁷	3.90 × 10 ⁻¹⁷	0.00%
A ₆	9.28 × 10 ⁻¹⁷	7.74 × 10 ⁻¹⁷	16.63%
A ₇	9.00 × 10 ⁻¹⁷	7.53 × 10 ⁻¹⁷	16.40%
A ₈	8.37 × 10 ⁻¹⁷	6.97 × 10 ⁻¹⁷	16.73%
A ₉	8.71 × 10 ⁻¹⁷	7.27 × 10 ⁻¹⁷	16.51%
A ₁₀	8.72 × 10 ⁻¹⁷	7.26 × 10 ⁻¹⁷	16.69%
A ₁₁	8.17 × 10 ⁻¹⁷	6.89 × 10 ⁻¹⁷	15.68%

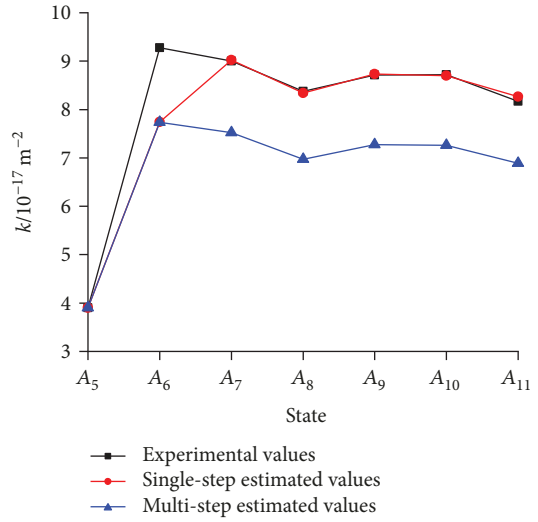


FIGURE 16: Comparison between the single-step estimation and multistep estimation.

\tilde{k}^{i-1} at the A_{i-1} state, which is a single-step estimation. Although the single-step estimation is highly precise, it largely depends on the test. To facilitate engineering applications, we estimate the permeability \tilde{k}^i at the A_i state by means of the estimated permeability value \tilde{k}^{i-1} at the A_{i-1} state and propose the following multistep estimation format for permeability:

$$k^{(M)} = k_0 \left(\frac{\phi^{(M)}}{\phi_0} \right)^{m_k},$$

$$\tilde{k}^{(M+1)} = k^{(M)} + \frac{\tilde{k}^{(M)}}{\phi^{(M)}} \left(\lambda_1^k \Delta \varepsilon_V^{(M+1)} + \lambda_2^k \Delta \gamma_{MC}^{(M+1)} \right),$$

$$\tilde{k}^{(i)} = \tilde{k}^{(i-1)} + \frac{\tilde{k}^{(i-1)}}{\phi^{(i-1)}} \left(\lambda_1^k \Delta \varepsilon_V^{(i)} + \lambda_2^k \Delta \gamma_{MC}^{(i)} \right),$$

$$i = M + 2, M + 3, \dots, N. \tag{55}$$

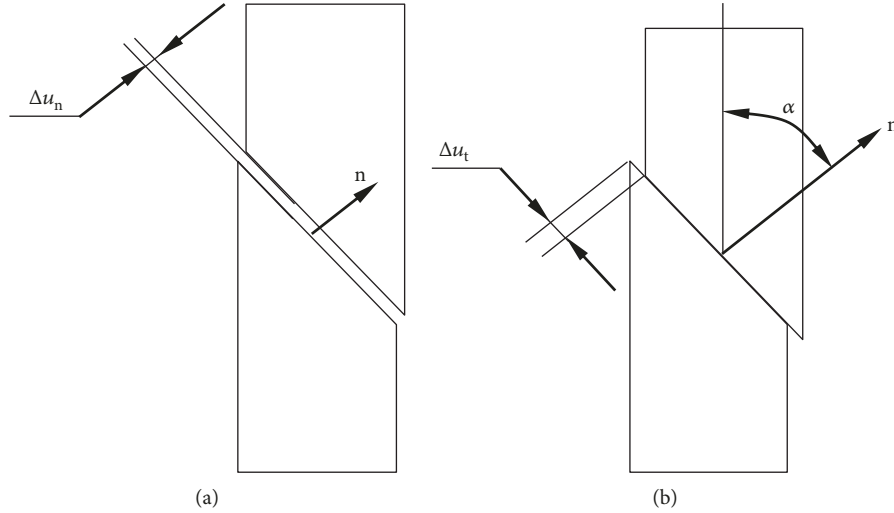


FIGURE 17: Relative displacement of the shear plane: (a) normal displacement and (b) tangential displacement.

TABLE 10: Values of axial stress, confining pressure, axial strain, circumferential strain, and permeability.

State	σ_1 (MPa)	σ_3 (MPa)	ε_1 (%)	ε_3 (%)	k (m ⁻²)	State
1	12.43	6.00	0.147	0.011	9.24×10^{-17}	Pre-peak
2	44.22	6.00	0.468	0.041	8.20×10^{-17}	Pre-peak
3	63.24	6.00	0.628	0.070	7.81×10^{-17}	Pre-peak
4	80.57	6.00	0.789	0.112	7.53×10^{-17}	Pre-peak
5	97.34	6.00	1.109	-0.195	6.97×10^{-17}	Shear yielding
6	40.65	6.00	1.124	-0.698	1.10×10^{-16}	Plastic flow
7	53.25	6.00	1.140	-0.758	1.15×10^{-16}	Plastic flow
8	44.56	6.00	1.116	-0.793	1.19×10^{-16}	Plastic flow
9	48.85	6.00	1.229	-0.800	1.14×10^{-16}	Plastic flow
10	35.56	6.00	1.125	-0.842	1.23×10^{-16}	Plastic flow
11	34.42	6.00	1.109	-0.845	$1.25E - 16$	Plastic flow

The values of permeability under the states A_6, A_7, \dots, A_{11} estimated by equation (55) are presented in Table 9.

Table 9 shows that the error between the estimated and experimental values of permeability is 16.6% at the stress state A_6 , while the errors obtained at the other stress states A_7, \dots, A_{11} are between 15.6% and 16.7%. Therefore, the iterative format represented by equation (55) is also generally stable.

Figure 16 shows a comparison of the multiple-step estimated values and the single-step estimated values of permeability. As shown in Figure 16, the multistep estimation at the stress state A_7 significantly differs from the single-step estimation (a difference of approximately 16.5%), and at later stress states, the error does not significantly increase.

The permeability model proposed in this paper can be used to only estimate the permeability after shear yielding. The variation in permeability after yielding is mainly caused by the relative displacement of the shear yield surface of the rock sample. Figure 17 shows the relative movement between

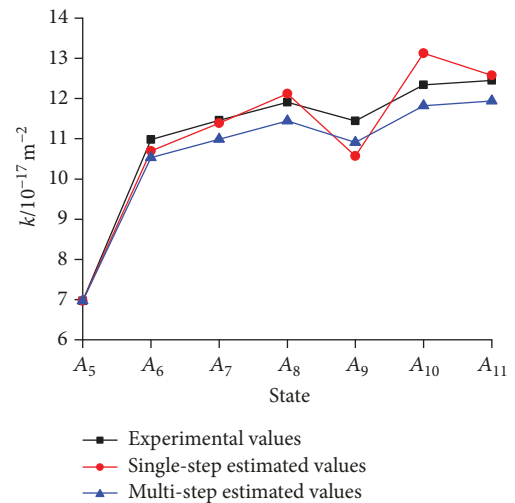


FIGURE 18: Comparison between experimental and estimated values under complete stress-strain process.

TABLE 11: Estimated values and relative errors of the permeability under complete stress-strain process.

State	Experimental values	Single-step estimated values	Permeability (m^{-2})		
			Relative error (%)	Multistep estimated values	Relative error (%)
A_5	6.79×10^{-17}	6.79×10^{-17}	—	6.79×10^{-17}	—
A_6	1.10×10^{-16}	1.07×10^{-16}	2.55%	1.07×10^{-16}	4.21%
A_7	1.15×10^{-16}	1.14×10^{-16}	0.61%	1.10×10^{-16}	4.13%
A_8	1.19×10^{-16}	1.21×10^{-16}	1.76%	1.14×10^{-16}	3.88%
A_9	1.14×10^{-16}	1.06×10^{-16}	7.60%	1.09×10^{-16}	5.01%
A_{10}	1.23×10^{-16}	1.31×10^{-16}	6.40%	1.18×10^{-16}	3.96%
A_{11}	1.25×10^{-16}	1.26×10^{-16}	1.04%	1.19×10^{-16}	4.05%

the shear yield surfaces of a rock sample. The relative displacement Δu_n in the normal direction of the shear plane results in the volumetric strain increment $\Delta \varepsilon_V^{(i)}$, and the relative displacement Δu_t in the shear plane results in the equivalent shear strain increment $\Delta \gamma_{MC}^{(i)}$, where $i = M + 1, M + 2, \dots, N$.

5.3. Applicability of Permeability Model for Plastic Flow. We conducted permeability tests of sandstone samples under the complete stress-strain process in order to fully verify the applicability of the permeability model for plastic flow. The test results are presented in Table 10. Iterative calculations are performed using equations (47) and (55) to obtain single-step estimated and multistep estimated values of permeability under every stress state after shear yielding, which are presented in Figure 18 and Table 11.

Table 11 shows that the errors between the single-step estimated values and the experimental values in the stress state A_7, \dots, A_{11} were from 0.61% to 7.60%. The errors between the multistep estimated values and the experimental values were from 3.88% to 5.01%. These errors indicate that the iterative format for estimating permeability, represented by equation (47) and (55), are generally stable.

6. Conclusions

Conventional triaxial compression tests were conducted on sandstone samples. A fluid flow test was conducted using the MTS 816.02 rock mechanics testing system and a self-designed permeation system to obtain the values of permeability under different stress states. The proposed iterative formats of the plastic multiplier and permeability estimations were based on the permeability model. The main conclusions were as follows:

- (1) A new plastic flow rule in the stress space was proposed based on the Mohr-Coulomb yield criterion and the isotropic hardening (softening) model. The plastic multiplier in each flow step after shear yielding was calculated, and the plastic multiplier was found to be positive under unloading conditions and negative under loading conditions

- (2) The equivalent shear strain increment in each flow step after shear yielding was calculated using the new plastic flow rule. The difference between estimated and experimental values of the equivalent shear strain increment was very small, which indicated that the new plastic flow rule is highly accurate
- (3) The permeability of the sandstone samples during the plastic state was estimated using the single-step and multistep estimation models. In the single-step estimation, the error between the estimated value and the experimental value of permeability was 16.5% at stress state A_6 , and the error in the remaining states was less than 1.2%. In the multistep estimation, the error between the estimated value and the experimental value of permeability was 16.6% at stress state A_6 , and the error was maintained between 15.6% and 16.7% in stress states A_7, \dots, A_{11} . These errors indicate that the iterative format of the multiple-step permeability estimation method is generally stable. The multiple-step permeability estimation model required the experimental value of permeability only at state A_5 , not the experimental values of permeability under states A_6, A_7, \dots, A_{11} . Therefore, the experimental value of permeability from state A_5 was used to estimate the permeability at states A_6, A_7, \dots, A_{11} . The multistep estimation method is therefore satisfactory for engineering applications and is highly precise
- (4) The influence coefficients of the volumetric strain increments and equivalent shear-strain increments of permeability were $\lambda_1^k = 2.55$ and $\lambda_2^k = 0.102$, respectively. Since $\lambda_2^k < \lambda_1^k$, the influence of the shear strain on permeability was less than that of the volumetric strain
- (5) In the flow step $A_9 \rightarrow A_{10}$, the volumetric strain increment was zero, and the magnitude of the increment of permeability was on the order of 1×10^{-20} , which is significantly smaller than those of the other five flow steps that have nonzero volumetric strain increments

- (6) The relative errors between the estimated values and the experimental values of permeability under complete stress-strain process are from 0.61% to 7.60%. The errors show that the permeability model for plastic flow is applicable

Symbols

A_i :	Stress states
a :	Limit of permeability when porosity tends to zero, $a = \lim_{\phi \rightarrow 0} k$
a_2 :	Coefficient to be determined
b :	Nondimensional coefficients
c :	Cohesion of sandstone
c_f :	Compressibility coefficient of the fluid
E :	Young's module of sandstone
F :	Plastic potential
H :	Height of sandstone sample
K_p :	Pore volume module
k :	Permeability
$\tilde{k}^{(i)}$:	Estimated value of permeability in the stress state A_i
Δk :	Permeability increment
m_k :	Nondimensional coefficients
N :	Number of stress states
n :	Total number of sampling
p :	Fluid pressure in fracture networks
p_1 :	Pressures in storage tank 1
p_2 :	Pressures in storage tank 2
p_{1f}, p_{2f} :	Pressure values of the two storage tanks at end of the sampling
q :	Mass flow of the fluid
S :	Cross-sectional area of sandstone sample
t_f :	Time of sampling end
Δu_n :	Relative displacement in the normal direction of the shear plane
Δu_t :	Relative displacement in the shear plane
V :	Volume of the storage tank
α :	Angle of shear failure
ε_1 :	Axial strain
ε_2 :	Radial strain
ε_3 :	Circumferential strain
$\Delta\varepsilon_1, \Delta\varepsilon_3$:	Strain increment
$\Delta\varepsilon_{1e}, \Delta\varepsilon_{3e}$:	Elastic-strain increments
$\Delta\varepsilon_{1p}, \Delta\varepsilon_{3p}$:	Plastic-strain increments
ε_V :	Volumetric strain
$\Delta\varepsilon_V$:	Volumetric strain increment
ϕ :	Porosity of sandstone sample
$\Delta\phi$:	Porosity increment
φ :	Internal friction angle
γ_{MC} :	Equivalent shear strain
$\Delta\gamma_{MC}$:	equivalent-shear-strain increment
$\tilde{\gamma}_{MC}$:	Estimated value of equivalent-shear strain
λ_1^k, λ_2^k :	Reflect the influence of volumetric strain and equivalent shear strain, respectively, on the permeability
Λ, G :	Lame coefficients
$\Delta\lambda_s$:	Plastic multiplier

μ :	Dynamic viscosity of the fluid
ν :	Poisson ratio
ρ :	Density of the fluid
σ :	Effective normal stress
σ_1 :	Axial stress
σ_2 :	Radial stress
σ_3 :	Circumferential stress
$\Delta\sigma_1, \Delta\sigma_3$:	Stress increment
σ_m :	Average principal stress
τ :	Sampling frequency
τ_{MC} :	Equivalent shear stress
v :	Flow velocity of the fluid.

Data Availability

The data that support the findings of this study are available from the corresponding author upon reasonable request.

Conflicts of Interest

The authors declare no conflict of interest.

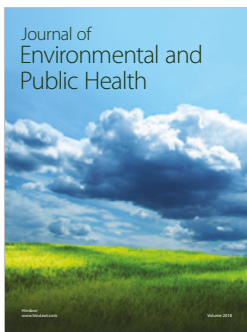
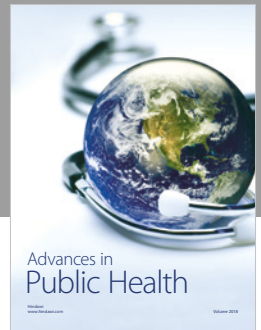
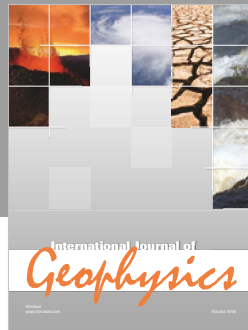
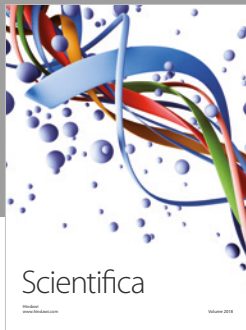
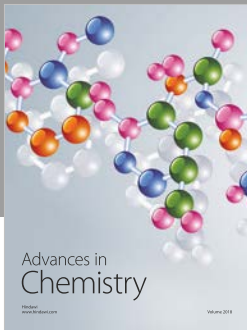
Acknowledgments

This work is based on the thesis which belongs to Dr. Xiaoyan Ni and supported by the Fundamental Research Funds for the Central Universities (Grant No. 2019QNA19).

References

- [1] X. Ni, Z. Chen, P. Wang, J. Wu, Y. Wu, and P. Gong, "Experimental investigation of the influence of differential stress, confining pressure and strain on aquifer sandstone permeability," *European Journal of Environmental and Civil Engineering*, vol. 8, pp. 1–16, 2018.
- [2] P. M. Doyen, "Permeability, conductivity, and pore geometry of sandstone," *Journal of Geophysical Research*, vol. 93, no. B7, pp. 7729–7740, 1988.
- [3] B. T. Ngwenya, O. Kwon, S. C. Elphick, and I. G. Main, "Permeability evolution during progressive development of deformation bands in porous sandstones," *Journal of Geophysical Research - Solid Earth*, vol. 108, no. B7, 2003.
- [4] V. Vajdova, P. Baud, and T. F. Wong, "Permeability evolution during localized deformation in Bentheim sandstone," *Journal of Geophysical Research - Atmospheres*, vol. 109, no. B10, article B10406, 2004.
- [5] M. R. Rezaee and C. M. Griffiths, "Pore geometry controls on porosity and permeability in the Tirrawarre Sandstone reservoir, Cooper basin, South Australia," in *American Association of Petroleum Geologists Annual Convention*, 5, p. 119, San Diego, CA, USA, 1996.
- [6] P. H. Nelson, "Permeability, porosity, and pore-throat size? A three-dimensional perspective," *Petrophysics*, vol. 46, pp. 452–455, 2005.
- [7] M. R. Rezaee, A. Jafari, and E. Kazemzadeh, "Relationships between permeability, porosity and pore throat size in carbonate rocks using regression analysis and neural networks," *Journal of Geophysics and Engineering*, vol. 3, no. 4, pp. 370–376, 2006.

- [8] A. M. S. Lala and N. A. A. El-Sayed, "Effect of pore framework and radius of pore throats on permeability estimation," *Journal of the African Earth Sciences*, vol. 110, pp. 64–74, 2015.
- [9] M. Zou, C. Wei, Z. Huang, and S. Wei, "Porosity type analysis and permeability model for micro-trans-pores, meso-macro-pores and cleats of coal samples," *Journal of Natural Gas Science and Engineering*, vol. 27, pp. 776–784, 2015.
- [10] W. E. Kenyon, "Petrophysical principles of applications of NMR logging," *The Log Analyst*, vol. 38, no. 2, pp. 21–43, 1997.
- [11] H. Pape, J. Arnold, R. Pechinig et al., "Permeability prediction for low porosity rocks by mobile NMR," *Pure and Applied Geophysics*, vol. 166, no. 5-7, pp. 1125–1163, 2009.
- [12] G. V. Chilinger, "Relationship between porosity, permeability, and grain-size distribution of sands and sandstones," *Developments in Sedimentology*, vol. 1, pp. 71–75, 1964.
- [13] I. G. Main, O. Kwon, B. T. Ngwenya, and S. C. Elphick, "Fault sealing during deformation-band growth in porous sandstone," *Geology*, vol. 28, no. 12, pp. 1131–1134, 2000.
- [14] J. A. Wang and H. D. Park, "Fluid permeability of sedimentary rocks in a complete stress-strain process," *Engineering Geology*, vol. 63, no. 3-4, pp. 291–300, 2002.
- [15] J. Q. Shi and S. Durucan, "Drawdown induced changes in permeability of coalbeds: a new interpretation of the reservoir response to primary recovery," *Transport in Porous Media*, vol. 56, no. 1, pp. 1–16, 2004.
- [16] J. Q. Shi and S. Durucan, "Exponential growth in San Juan Basin Fruitland coalbed permeability with reservoir drawdown model match and new insights," *SPE Reservoir Evaluation and Engineering*, vol. 13, no. 6, pp. 914–925, 2013.
- [17] Z. Pan and L. D. Connell, "Modelling permeability for coal reservoirs: a review of analytical models and testing data," *International Journal of Coal Geology*, vol. 92, pp. 1–44, 2012.
- [18] L. D. Connell, "Coupled flow and geomechanical processes during gas production from coal seams," *International Journal of Coal Geology*, vol. 79, no. 1-2, pp. 18–28, 2009.
- [19] Y. Meng, Z. Li, and F. Lai, "Experimental study on porosity and permeability of anthracite coal under different stresses," *Journal of Petroleum Science and Engineering*, vol. 133, pp. 810–817, 2015.
- [20] C. R. McKee, A. C. Bumb, and R. A. Koenig, "Stress-dependent permeability and porosity of coal and other geologic formations," *SPE Formation Evaluation*, vol. 3, no. 1, pp. 81–91, 1988.
- [21] Z. Zhang, R. Zhang, H. Xie, and M. Gao, "The relationships among stress, effective porosity and permeability of coal considering the distribution of natural fractures: theoretical and experimental analyses," *Environment and Earth Science*, vol. 73, no. 10, pp. 5997–6007, 2015.
- [22] P. L. P. Wasantha, W. J. Darlington, and P. G. Ranjith, "Characterization of mechanical behaviour of saturated sandstone using a newly developed Triaxial apparatus," *Experimental Mechanics*, vol. 53, no. 5, pp. 871–882, 2013.
- [23] C. Louis, *Study of Groundwater Flow in Jointed Rock and Its Influence on the Stability of Rock Masses*, Imperial College of Science and Technology, London, 1969.
- [24] D. T. Snow, "Anisotropic permeability of fractured media," *Water Resources Research*, vol. 5, no. 6, pp. 1273–1289, 1969.
- [25] P. M. T. M. Schutjens and H. D. de Ruig, "The influence of stress path on compressibility and permeability of an overpressurised reservoir sandstone: some experimental data," *Physics and Chemistry of the Earth*, vol. 22, no. 1-2, pp. 97–103, 1997.
- [26] D. W. Rhett and L. W. Teufel, "Effect of reservoir stress path on compressibility and permeability of sandstones," in *SPE Annual Technical Conference and Exhibition*, Washington, DC, USA, 1992.
- [27] J. Heiland, "Laboratory testing of coupled hydro-mechanical processes during rock deformation," *Hydrogeology Journal*, vol. 11, no. 1, pp. 122–141, 2003.
- [28] B. Han, S. Y. Xie, and J. F. Shao, "Experimental investigation on mechanical behavior and permeability evolution of a porous limestone under compression," *Rock Mechanics and Rock Engineering*, vol. 49, no. 9, pp. 3425–3435, 2016.
- [29] J. Bear, *Dynamics of Fluids in Porous Media*, Elsevier, New York, NY, USA, 1972.
- [30] P. A. Witherspoon, J. S. Y. Wang, K. Iwai, and J. E. Gale, "Validity of cubic law for fluid flow in a deformable rock fracture," *Water Resources Research*, vol. 16, no. 6, pp. 1016–1024, 1980.
- [31] P. G. Ranjith and D. R. Viete, "Applicability of the 'cubic law' for non-Darcian fracture flow," *Journal of Petroleum Science and Engineering*, vol. 78, no. 2, pp. 321–327, 2011.
- [32] M. Javadi, M. Sharifzadeh, K. Shahriar, and Y. Mitani, "Critical Reynolds number for nonlinear flow through rough-walled fractures: the role of shear processes," *Water Resources Research*, vol. 50, no. 2, pp. 1789–1804, 2014.
- [33] J. Heiland, "Permeability of triaxially compressed sandstone: influence of deformation and strain-rate on permeability," *Pure and Applied Geophysics*, vol. 160, no. 5, pp. 889–908, 2003.
- [34] H. Wang and W. Xu, "Relationship between permeability and strain of sandstone during the process of deformation and failure," *Geotechnical and Geological Engineering*, vol. 31, no. 1, pp. 347–353, 2013.
- [35] R. M. Bustin, X. J. Cui, and L. Chikatamarla, "Impacts of volumetric strain on CO₂ sequestration in coals and enhanced CH₄ recovery," *American Association of Petroleum Geologists Bulletin*, vol. 92, no. 1, pp. 15–29, 2008.
- [36] H. H. Liu, J. Rutqvist, and J. G. Berryman, "On the relationship between stress and elastic strain for porous and fractured rock," *International Journal of Rock Mechanics and Mining Sciences*, vol. 46, no. 2, pp. 289–296, 2009.
- [37] R. E. Goodman, *Introduction to Rock Mechanics*, John Wiley & Sons, New York, NY, USA, 2nd edition, 1989.
- [38] K. S. Carney, D. J. Benson, P. Dubois, and R. Lee, "A phenomenological high strain rate model with failure for ice," *International Journal of Solids and Structures*, vol. 43, no. 25-26, pp. 7820–7839, 2006.
- [39] J. Lubliner and B. Moran, "Plasticity theory," *Journal of Applied Mechanics*, vol. 59, no. 1, p. 245, 1992.
- [40] H.-C. Wang, W.-H. Zhao, D.-S. Sun, and B.-B. Guo, "Mohr-Coulomb yield criterion in rock plastic mechanics," *Chinese Journal of Geophysics*, vol. 55, no. 6, pp. 733–741, 2012.
- [41] Itasca, "FLAC. Fast Lagrangian analysis of continua. Version 5.0. Minneapolis, Minnesota," 2005, <https://www.itascacg.com>.
- [42] H. Bai, D. Ma, and Z. Chen, "Mechanical behavior of groundwater seepage in karst collapse pillars," *Engineering Geology*, vol. 164, pp. 101–106, 2013.



Hindawi

Submit your manuscripts at
www.hindawi.com

